



1                   **Permian-Triassic redox shift and its ferruginous**  
2                   **aftermath in epicontinental seas**

3       Fen Yang<sup>1,2</sup>, Sen Li<sup>3\*</sup>, Stephen E. Grasby<sup>4</sup>, David Bond<sup>5</sup>, Ming Pan<sup>1,2</sup>, Yadong Sun<sup>3</sup>

4       <sup>1</sup> Institute of Karst Geology, CAGS/Key Laboratory of Karst Dynamics, MNR & GZAR/International  
5       Research Center on Karst under the Auspices of UNESCO, Guilin, Guangxi 541004, China 541004,  
6       China.

7       <sup>2</sup> Pingguo Guangxi, Karst Ecosystem, National Observation and Research Station, Pingguo, Guangxi  
8       531406, China.

9       <sup>3</sup> State Key Laboratory of Geomicrobiology and Environmental Changes, China University of  
10       Geosciences, Wuhan 430074, China.

11       <sup>4</sup> Geological Survey of Canada, 3303-33rd Street NW, Calgary, Alberta T2L 2A7, Canada.

12       <sup>5</sup> School of Environmental and Life Sciences, University of Hull, Hull, HU6 7RX, United Kingdom.

13       *Correspondence to:* Sen Li (lisen@cug.edu.cn)

14       **Abstract.** Marine anoxia has been implicated as a key environmental driver of the end-Permian mass  
15       extinction (EPME) and the subsequent prolonged recovery. However, the spatial and temporal extent of  
16       oxygen limitation during the EPME interval remains contentious. Here, we present iron speciation, pyrite  
17       framboid and molybdenum-uranium (Mo-U) covariation data from two palaeogeographically distinct  
18       settings: the Tethyan Chibi section (South China) and the Panthalassian Ursula Creek section (Western  
19       Canada) to evaluate redox dynamics across the Permian-Triassic transition. Our data suggest that bottom  
20       waters were predominantly dysoxic during the late Changhsingian at both sites. Later, the prevalence of  
21       small pyrite framboids, elevated Mo and U enrichment factors ( $Mo_{EF}$  and  $U_{EF}$ ), and high  $Mo_{EF}/U_{EF}$  ratios  
22       near the EPME horizon implicate seafloor anoxia as a key trigger for marine extinctions in epicontinental  
23       seas. In the post-extinction Early Triassic, iron speciation and  $Mo_{EF}-U_{EF}$  covariation data reveal a shift  
24       to persistently ferruginous conditions in both locations. A global compilation of iron speciation data  
25       indicates that anoxic conditions fluctuated between ferruginous and euxinic in epicontinental seas during  
26       the Permian-Triassic crisis, with ferruginous conditions expanding significantly in the earliest Triassic.  
27       The expansion of a ferruginous seafloor would have limited phosphorus bioavailability, suppressing  
28       primary productivity in the immediate aftermath of the EPME, thereby contributing to the slow recovery.



## 29 **1 Introduction**

30 The end-Permian mass extinction (EPME), ca. 252 Ma, stands as the Phanerozoic's most profound  
31 biodiversity crisis and results in a major turnover from Paleozoic to Mesozoic ecosystems (Sepkoski,  
32 1981; Erwin, 2006). An extreme greenhouse climate prevailed during the Early Triassic (Joachimski et  
33 al., 2012; Sun et al., 2012), accompanied by extensive oxygen depletion (Isozaki, 1997; Bond and  
34 Wignall, 2010; Lau et al., 2016). The post-extinction recovery of marine ecosystems was protracted and  
35 punctuated by a series of aborted recoveries, initially characterized by low-complexity communities  
36 dominated by calcimicrobes and sparse, low-diversity metazoans. Opportunistic taxa (e.g., small  
37 gastropods and bivalves) proliferated globally (Pruss et al., 2006; Chen and Benton, 2012; Foster and  
38 Twitchett, 2014).

39 Marine anoxia has been widely considered a primary mechanism driving the EPME and the  
40 subsequent slow, punctuated biotic recovery (Wignall and Hallam, 1992; Takahashi et al., 2009; Grasby  
41 et al., 2013). Several competing hypotheses describe the spatio-temporal patterns of oxygen depletion  
42 during the EPME. These include the development of global "superanoxia" (Isozaki, 1997; Wignall and  
43 Twitchett, 2002), the stratification of oceans into oxic surface waters and euxinic (H<sub>2</sub>S-rich) deep waters  
44 separated by a stable chemocline (e.g., Kump et al., 2005; Meyer et al., 2008), and the expansion of  
45 ferruginous [Fe(II)-rich, non-euxinic] conditions (Clarkson et al., 2016). Multiple geochemical proxies  
46 point towards the development of persistent or episodic euxinic conditions in Panthalassa and in  
47 epicontinental basins. In deep-water settings of Panthalassa (e.g., the rare records of Japan and New  
48 Zealand), small pyrite framboids (mean diameters < 5 μm), significant concentrations of redox-sensitive  
49 trace elements such as Mo, and negative pyrite sulfur isotope shifts are all indicative of persistent euxinia  
50 and restricted water-column ventilation (Shen et al., 2011; Takahashi et al., 2021). Numerous studies  
51 demonstrate that euxinic waters invaded shallow epicontinental basins extensively around the Permian-  
52 Triassic (P-T) boundary, including equatorial Tethys (e.g., the South China Block), the Gondwanan  
53 margin in mid to high latitudes, and the Pangaea northwestern margin (Wignall and Twitchett, 1996;  
54 Neilsen et al., 2010; Grasby and Beauchamp, 2008, Lau et al., 2016; Zhang et al., 2017; Stebbins et al.,  
55 2019; Xiang et al., 2020). Biomarker evidence from chlorobactene (indicative of green sulfur bacteria)  
56 suggests that euxinic waters expanded into the photic zone (Grice et al., 2005; Cao et al., 2009).

57 In contrast, iron proxies reveal dynamic redox fluctuations between euxinic and ferruginous



58 conditions, exhibiting regional heterogeneity during the EPME. Along the margins of equatorial Tethys  
59 (e.g., South China), iron proxies document a shift from the Changhsingian euxinic to Griesbachian  
60 ferruginous conditions, as indicated by decreased the proportion of iron bound in pyrite relative to the  
61 highly reactive iron pool ( $Fe_{py}/Fe_{HR}$ ) in multiple stratigraphic records (Xiang et al., 2016, 2020; Lei et  
62 al., 2017; Ge et al., 2022). Conversely, strata from the northwestern Pangaea margin reveal a different  
63 redox trend, with ferruginous conditions transitioning to euxinic environments across the P-T boundary  
64 (e.g., Neilsen et al., 2010; Mettam et al., 2017; Schobben et al., 2020). Meanwhile, Panthalassa  
65 experienced predominantly euxinic conditions across the EPME, with intermittent ferruginous intervals  
66 developing during the earliest Triassic (Takahashi et al., 2021).

67 Evidence increasingly suggests that anoxia may have been largely confined to slope settings, with  
68 periodic redox oscillations driving transient anoxic episodes in shallow marine environments (Algeo et  
69 al., 2010; Shen et al., 2012, 2016; Zhang et al., 2017). Multiple independent proxies—including  
70 bioturbation, depletion of  $Fe_{HR}$ , absence of pyrite framboids, rare earth element anomalies, and Mo and  
71 Tl isotope signatures—indicate intervals with sustained oxygenation of bottom waters regionally around  
72 the EPME (Beatty et al., 2008; Proemse et al., 2013; Garbelli et al., 2016; Newby et al., 2021; Chen et  
73 al., 2022; Ge and Bond, 2022; Taniwaki et al., 2022; Yang et al., 2024; Frank et al., 2025). These findings  
74 challenge the paradigm of globally pervasive anoxia, suggesting instead that oxygen restriction during  
75 the EPME was more spatially heterogeneous than previously suggested. While oxic refugia can be  
76 reconciled with U-based modelling that suggests only ~20% of the seafloor was anoxic at that time (Lau  
77 et al., 2016), there remains an issue that the residence time of U in sea water would not capture transient  
78 anoxic events (Grasby et al., 2021).

79 To further resolve spatial-temporal changes in marine redox states during the EPME, we  
80 investigated two Upper Permian to Lower Triassic successions from contrasting palaeogeographic  
81 locations: Chibi (equatorial Tethys) and Ursula Creek (northwestern margin of Pangaea). We then  
82 synthesize multi-proxy data to evaluate the redox history through the EPME and earliest Triassic in  
83 differing settings.

## 84 **2 Geological settings**

85 Paleogeographic reconstructions indicate that the South China Block was situated in the equatorial



86 eastern Tethys and remained tectonically isolated during the P-T interval (Scotese, 2014; Fig. 1A).  
87 During the late Permian (Changhsingian), sedimentation across the South China Block was  
88 characterized by a pronounced platform-basin differentiation, with shallow-water carbonate deposition  
89 dominating the Yangtze Platform and siliceous deep-water sediments accumulating along its margins  
90 (Feng et al., 1996; Fig. 1B). The Chibi study section (29°45'5.33"N, 113°57'6.75"E) is exposed in the  
91 northern marginal basin of the middle Yangtze Platform. It records a continuous P-T stratigraphic  
92 succession, encompassing the Wuchiaping and Talung formations (Upper Permian) and extending  
93 upward into the Daye Formation (Lower Triassic) (Yang et al., 2022). The Wuchiaping Formation  
94 comprises grey, thick-bedded wackestones and packstones containing abundant benthic calcareous  
95 bioclasts and chert nodules. It is overlain by the Talung Formation, which is characterized by thin-bedded  
96 cherts interbedded with siliceous mudstones, wackestones, and shales and commonly yields radiolarians  
97 and sponge spicules. The overlying Daye Formation consists mainly of thin-bedded wackestones  
98 interlayered with marls, and the P-T boundary is located 83 cm above its basal contact (Yang et al., 2022).

99 The Ursula Creek section (55°59'36.54"N, 123°10'27.18"W) is located on the north shore of  
100 Williston Lake, a hydroelectric reservoir in British Columbia in the Canadian Rocky Mountains (Fig.  
101 1C). Palaeogeographically, the Ursula Creek section was located on the Pangaea northwestern margin  
102 (approximately 30° N) during the P-T interval (Fig. 1A). Previous studies have documented the  
103 stratigraphic characteristics of the Ursula Creek section, a deep marine succession that exposes near-  
104 vertically dipping strata spanning the Middle Permian to Middle Triassic (Henderson, 1997; Woods et  
105 al., 2023). Upper Permian-Lower Triassic strata are assigned to the Fantasque and Grayling formations.  
106 The Fantasque Formation is composed predominantly of thinly bedded cherts intercalated with shale  
107 layers, and its faunal assemblages are characterized by abundant radiolarians and sponge spicules. The  
108 overlying Grayling Formation comprises thinly bedded shales. The P-T boundary was identified at ~80  
109 cm above the base of the Grayling Formation (Wignall and Newton, 2003).

### 110 **3 Methods**

111 Size distributions of pyrite framboids were determined from 37 prepared thin sections at Ursula Creek  
112 using a scanning electron microscope (SEM) at the State Key Laboratory of Geomicrobiology and  
113 Environmental Changes, China University of Geosciences (CUG Wuhan). All polished thin sections



114 were sputter-coated with carbon powder to enhance imaging quality. The SEM was operated in  
115 backscattered electron mode at  $2500 \times$  magnification. The chemical composition of framboids was  
116 qualitatively characterized using energy-dispersive spectroscopy (EDS).

117 For iron proxies, 97 bulk rock samples from the Chibi and Ursula Creek sections were crushed with  
118 a jaw crusher and ground by a mixer mill. Total iron ( $Fe_T$ ) concentrations were determined using X-ray  
119 fluorescence (XRF) at the ALS Minerals laboratory located in Guangzhou, achieving a reproducibility  
120 better than 0.1 wt% ( $1\sigma$ ). Of these, 54 samples showing  $Fe_T$  values above 0.5 wt% were used in  
121 subsequent Fe speciation extractions. Iron phases associated with carbonates ( $Fe_{carb}$ ), (oxyhydr)oxides  
122 ( $Fe_{ox}$ ), and magnetite ( $Fe_{mag}$ ) were sequentially extracted following Poulton and Canfield (2005).  $Fe_{carb}$   
123 was removed using 1M Na-acetate (pH 4.5) at 50 °C for 48 h,  $Fe_{ox}$  with Na-dithionite (pH 4.8) at room  
124 temperature for 2h, and  $Fe_{mag}$  with a solution of 0.2M ammonium oxalate and 0.17M oxalic acid at  
125 room temperature for 6h. Fe concentrations were determined using atomic absorption spectrometry at  
126 the State Key Laboratory of Geomicrobiology and Environmental Changes, CUG Wuhan. The  $Fe_{py}$  was  
127 quantified stoichiometrically determined by the weight of precipitated  $Ag_2S$  following chromous  
128 chloride distillation, as described by Canfield et al. (1986). Replicate extractions of the WHIT  
129 international reference material (Alcott et al., 2020) gave a relative standard deviation below 5% for each  
130 step.

131 For trace elements, 75 powdered samples were treated with a mixture of  $H_2O$ , HF,  $HClO_4$ , and  
132  $HNO_3$  (2:2:1:1) for digestion at the Geological Survey of Canada. Analyses of the resulting solutions  
133 were quantified by ICP-MS (PerkinElmer), and replicate measurements showed a relative deviation  
134 below 2% ( $2\sigma$ ). Enrichment factors (EF) for trace elements were obtained by normalizing the sample  
135 X/Al ratios to those of the Post-Archean Average Shale (PAAS; Taylor and McLennan, 1985), with X  
136 representing Mo and U.

## 137 4 Results

### 138 4.1 Pyrite framboid analysis

139 At Ursula Creek, abundant pyrite framboids were observed in 20 of the 37 samples (54.1%; Fig. 2),  
140 totaling 2140 individuals measured for this study (see supplementary material). The remaining 17  
141 samples contained either none, or rare pyrite framboids and euhedral pyrite.



142 Mean framboid diameters generally decrease upward in the Fantasque Formation (Fig. 2). Within  
143 the lowermost 3 m of the study section, three samples yield mean framboid diameters of 7.9–9.6  $\mu\text{m}$ ,  
144 with standard deviation ( $1 \sigma$ ) ranging from 2.0 to 3.2  $\mu\text{m}$  (Fig. 3). At section height 3–10 m, pyrite  
145 framboids are mostly absent except for one sample containing a small quantity ( $n = 55$ ) of larger  
146 framboids (mean = 10.4  $\mu\text{m}$ ), a wide size distribution (3.6–25.3  $\mu\text{m}$ ), and a standard deviation of 4.7  $\mu\text{m}$ .  
147 Numerous framboids are observed within the upper interval of the Fantasque Formation (10–13 m section  
148 height), with mean diameters ranging from 6.8 to 9.6  $\mu\text{m}$  and standard deviations between 2.1 and 3.5  
149  $\mu\text{m}$ . Mean diameters decrease slightly at the top of the Fantasque Formation (13–14.3 m section height),  
150 ranging from 5.7 to 6.5  $\mu\text{m}$ , with narrow size distribution ( $1 \sigma < 3.0 \mu\text{m}$ ). Within the basal ~2.7 m of the  
151 overlying Grayling Formation shales (earliest Griesbachian), framboids are absent. Above this interval,  
152 numerous small pyrite framboids exist in the Grayling Formation (17.5–31.6 m section height), with  
153 mean diameters between 5.3 and 6.5  $\mu\text{m}$  and  $1 \sigma$  from 1.2 to 2.8  $\mu\text{m}$ . EDS analysis detected about 25 wt%  
154 oxygen content in pyrite framboids from the Ursula Creek section (Figs. 4A and B), suggesting partial  
155 oxidation rather than stoichiometric  $\text{FeS}_2$ .

#### 156 **4.2 $\text{Fe}_T$ , $\text{Fe}_T/\text{Al}$ and Fe proxies**

157 At Ursula Creek,  $\text{Fe}_T$  contents range from 0.2 to 4.7 wt% (mean = 1.3 wt%), with 46 out of 59 samples  
158 exceeding 0.5 wt% (Fig. 2). Samples exhibiting  $\text{Fe}_T < 0.5$  wt% occur exclusively in the lower Fantasque  
159 Formation (Fig. 2).  $\text{Fe}_T$  concentrations in the upper Fantasque Formation show a slight increase, varying  
160 from 0.5 to 1.1 wt% (mean = 0.7 wt%). The Grayling Formation exhibits generally higher  $\text{Fe}_T$  (0.5–4.7  
161 wt%, mean = 2.2 wt%). In samples with  $\text{Fe}_T > 0.5$  wt%, the  $\text{Fe}_{\text{HR}}/\text{Fe}_T$  is generally above 0.6 (mean = 0.9),  
162 with one exception of 0.3. The  $\text{Fe}_{\text{py}}/\text{Fe}_{\text{HR}}$  are low, varying from 0 to 0.7 (mean = 0.1). The Fantasque  
163 Formation shows consistently low  $\text{Fe}_{\text{py}}/\text{Fe}_{\text{HR}}$  ratios (mean = 0.2) while the Grayling Formation has more  
164 variable  $\text{Fe}_{\text{py}}/\text{Fe}_{\text{HR}}$  ratios (0–0.5, mean = 0.1). Notably, the Ursula Creek section records elevated  $\text{Fe}_{\text{ox}}$   
165 contents, and  $\text{Fe}_{\text{ox}}/\text{Fe}_{\text{HR}}$  ratios span 0.1–0.9, with 28 of 35 values exceeding 0.5. The  $(\text{Fe}_{\text{ox}} + \text{Fe}_{\text{py}})/\text{Fe}_{\text{HR}}$   
166 ratios fall within 0.6–0.9 (mean = 0.8), with only two samples displaying values below 0.6. The total Fe  
167 relative to aluminum ( $\text{Fe}_T/\text{Al}$ ) ratios vary from 0.1 to 2.7 (mean = 0.5), averaging 0.4 in the Fantasque  
168 Formation and 0.5 in the more variable Grayling Formation.

169 At Chibi,  $\text{Fe}_T$  concentrations vary from 0.1–5.7 wt% (mean = 1.1 wt%), with 25 samples showing  
170 values  $> 0.5$  wt% (Fig. 5). Among these, 19 samples were analyzed for iron speciation. Most samples



171 from the lower to middle Talung Formation (*C. subcarinata* and *C. changxingensis* zones) yield  $Fe_T <$   
172 0.5 wt%.  $Fe_T$  concentrations increase markedly in the upper Talung Formation (*C. yini-H. praeparvus*  
173 Zone), ranging from 0.9 to 5.7 wt%. The Daye Formation generally contained higher  $Fe_T$  concentrations  
174 than the Talung Formation, with most samples ranging from 0.5 to 2.6 wt% and two samples showing  
175 lower values. For samples with  $Fe_T > 0.5$  wt%,  $Fe_{HR}/Fe_T$  ratios fall between 0.4 to 1.0 (mean = 0.7). The  
176  $Fe_P/Fe_{HR}$  ratios in this section span 0.1–0.9 (mean = 0.4), with most values  $< 0.6$  (14 out of 19 samples).  
177  $Fe_{ox}$  contents are low, with  $Fe_{ox}/Fe_{HR}$  ratios  $< 0.1$  in all samples. The  $Fe_T/Al$  ratios fall between 0.4 and  
178 6.7, (mean = 1.0) averaging 2.1 in the Talung Formation and a more stable 0.6 in the lower Daye  
179 Formation.

#### 180 4.3 Molybdenum and uranium concentrations, enrichment factors and ratios (Ursula Creek)

181 At Ursula Creek, Mo and U concentrations, their enrichment factors ( $Mo_{EF}$ ,  $U_{EF}$ ), and corresponding  
182 ratios ( $Mo/U$ ,  $Mo_{EF}/U_{EF}$ ) display similar variations, generally rising from the Late Permian into the Early  
183 Triassic (Fig. 2). In the Fantasque Formation ( $n = 34$ ), Mo concentrations fall between 0.1 and 4.8 ppm  
184 (mean = 0.7 ppm), with corresponding  $Mo_{EF}$  values span 0.6 to 25.6 (mean = 4.3); most samples ( $n = 31$ )  
185 show only modest Mo enrichment ( $Mo_{EF} < 10$ ). For U, concentrations fall in the range of 0.2–2.2 ppm  
186 (mean = 1.0 ppm), and  $U_{EF}$  values range from 1.6 to 17.7 (mean = 6.1).  $Mo_{EF}/U_{EF}$  ratios are generally  
187 low (0.2–2.2, mean = 0.6), with 25 samples exhibiting values below 0.1 times that of modern seawater,  
188 and the remainder falling in the range of 0.1 to 0.3 times seawater (Fig. 6). In contrast,  $Mo/U$  ratios are  
189 relatively higher than  $Mo_{EF}/U_{EF}$  ratios, spanning 0.2–2.4 (mean = 0.7).

190 In the Grayling Formation ( $n = 41$ ), all proxies exhibit significantly higher values. For Mo,  
191 concentrations and enrichment factors show significantly greater variation from 0.6 to 146.8 ppm (mean  
192 = 20.0 ppm) and 2.2 to 175.2 (mean = 29.1), respectively. Most samples ( $n = 36$ ) show high Mo  
193 enrichment ( $Mo_{EF}$ : 11.0 to 57.0). One sample displays an extremely high enrichment ( $Mo_{EF} > 100$ ), and  
194 four samples show low to modest enrichment ( $Mo_{EF} < 10$ ). In contrast to Mo, U concentrations and  
195 enrichment factors exhibit modest variability, with concentrations varying narrowly from 1.3 to 15.0 ppm  
196 (mean = 6.0 ppm) and  $U_{EF}$  values ranging from 4.6 to 23.4 (mean = 9.9).  $Mo_{EF}/U_{EF}$  ratios fall between  
197 0.4 and 8.9 (mean = 2.9). All but one sample have  $Mo_{EF}/U_{EF}$  ratios between 0.1 and 1 times that of  
198 modern seawater (Fig. 6).  $Mo/U$  ratios span 0.5–9.8 (mean = 3.1).



199 **5 Discussion**

200 **5.1 Redox evolution**

201 Among various geochemical and sedimentological proxies for distinguishing redox states, pyrite  
202 framboid mean size has become established as a reliable method (e.g., Wilkin and Barnes, 1996). The  
203 abundance of pyrite framboids typically increases as anoxia develops, accompanied by a decrease in  
204 mean diameter and a narrowing of the size distribution. Specifically, the absence of framboids typically  
205 indicates local oxic conditions; abundant framboids with mean diameters ranging from 6 to 10  $\mu\text{m}$   
206 suggest dysoxic conditions; abundant framboids with mean diameters below 6  $\mu\text{m}$  reflect anoxic  
207 environments, with those below 5  $\mu\text{m}$  pointing to euxinic settings (e.g., Wilkin and Barnes, 1996; Bond  
208 and Wignall, 2010).

209 Iron speciation [e.g., Fe(II), Fe(III), and sulfide-associated phases] exhibits redox-sensitive  
210 geochemical behavior, which is widely applied as a proxy to reconstruct palaeo-redox states in ancient  
211 depositional settings (e.g., Poulton and Canfield, 2011). To ensure analytical reliability, these proxies are  
212 typically applied only to samples with  $\text{Fe}_T$  concentrations  $> 0.5$  wt% (Clarkson et al., 2014). Modern  
213 oxic marine sediments typically exhibit a depletion of  $\text{Fe}_{\text{HR}}$ , as indicated by  $\text{Fe}_{\text{HR}}/\text{Fe}_T < 0.22$ , which  
214 reflects limited authigenic Fe preservation under well-oxygenated conditions (Poulton and Raiswell,  
215 2002). By contrast, under anoxic environments, sediments commonly show substantial enrichment of  
216  $\text{Fe}_{\text{HR}}$  ( $\text{Fe}_{\text{HR}}/\text{Fe}_T > 0.38$ ; Poulton, 2021). Accumulation of  $\text{H}_2\text{S}$  in anoxic bottom waters promotes  
217 pyritization of  $\text{Fe}_{\text{HR}}$ , driving  $\text{Fe}_{\text{py}}/\text{Fe}_{\text{HR}} > 0.8$ , an established threshold for euxinic settings. Conversely,  
218  $\text{Fe}_{\text{py}}/\text{Fe}_{\text{HR}} < 0.6$  is indicative of ferruginous settings, where  $\text{H}_2\text{S}$  availability is limited. When  $\text{Fe}_{\text{py}}/\text{Fe}_{\text{HR}}$   
219 falls between 0.6 and 0.8, the redox classification becomes ambiguous and further evidence is required  
220 (e.g., from independent proxies) to make an informed interpretation (Poulton and Canfield, 2011).

221 Molybdenum-uranium covariation is widely used to reconstruct palaeo-redox states in ancient  
222 depositional environments, owing to the distinct redox-sensitive geochemical behaviors of these  
223 elements (e.g., Algeo and Tribovillard, 2009). The application of  $\text{Mo}_{\text{EF}}$  and  $\text{U}_{\text{EF}}$  to non-siliciclastic rocks  
224 is subject to potential artifacts, as low detrital Al content can result in elevated values (Tribovillard et al.,  
225 2006). Nevertheless, the consistent stratigraphic trends in EFs, elemental concentrations, and their ratios  
226 in this study support their reliable application in redox analysis (Fig. 2). Generally, more reducing  
227 conditions promote greater enrichment of both elements in sediments, with Mo uptake increasing more



228 rapidly than that of U. Under oxic conditions, both Mo and U show little or no enrichment. In dysoxic  
229 environments, Mo and U typically show low and modest enrichment factors ( $EFs < 10$ ), and U tends to  
230 be more enriched than Mo ( $U_{EF} > Mo_{EF}$ ) as a result of U being incorporated near the Fe(II)–Fe(III) redox  
231 transition, whereas Mo enrichment generally depends on the availability of free  $H_2S$ . Under oxygen-  
232 depleted, non-euxinic conditions, both elements exhibit stronger enrichment ( $EFs > 10$ ), with  $Mo_{EF}/U_{EF}$   
233  $< 1 \times$  seawater. In contrast, under euxinic conditions characterized by abundant  $H_2S$  in the water column,  
234 both elements exhibit strong enrichment ( $EFs > 10$ ); however, Mo is preferentially accumulated, leading  
235 to  $Mo_{EF}/U_{EF} > 1 \times$  seawater.

236 Redox proxies from the Ursula Creek section indicate prolonged water-column deoxygenation  
237 during the Changhsingian at the northwestern margin of Pangaea. Abundant pyrite framboids with  
238 relatively large mean diameters (7.9 to 9.6  $\mu m$ ), and low  $Mo_{EF}/U_{EF}$  ratios ( $< 0.1 \times$  seawater) in the basal  
239 ~3 meters of the studied Fantasque Formation indicate dysoxic conditions prevailed during deposition  
240 (Figs. 2 and 6; Bond and Wignall, 2010; Tribovillard et al., 2012). Though this interval is characterized  
241 by low  $Mo_{EF}$  (1.0 to 3.8) and low to modest  $U_{EF}$  (2.3 to 13.4), the low detrital Al component (0.6 to 2.4  
242 wt%) typical for (bio)chemical sediments (e.g., chert and pure carbonate) results in EF values that appear  
243 higher than those in siliciclastic sediments (Tribovillard et al., 2006). From 3 to 8.5 m section height  
244 (Fantasque Formation), intense bioturbation, including ichnotaxa belonging to *Diplocraterion*,  
245 *Teichichnus*, and *Planolites*, along with low  $Mo_{EF}$  (0.7 to 9.0) and  $U_{EF}$  (1.9 to 7.1) values, low Al contents  
246 (0.6 to 2.5 wt%), low  $Mo_{EF}/U_{EF}$  ratios ( $< 0.1 \times$  seawater), and a general lack of pyrite framboids suggests  
247 that oxic to dysoxic bottom waters were established during this part of the Changhsingian (Wignall and  
248 Newton, 2003; Fig. 2). Several samples that lack pyrite framboids at a height of 8.5–10 m exhibit  
249  $Fe_{HR}/Fe_T > 0.38$ , moderately elevated  $Mo_{EF}$  (17.4 to 25.6) and  $U_{EF}$  (11.7–17.7), with  $Mo_{EF}/U_{EF}$  ratios  
250 spanning 0.1 to 0.3 times that of seawater, suggestive of anoxic conditions. Considering partial pyrite  
251 oxidation detected by EDS (Fig. 4A), it is possible that using  $Fe_{py}/Fe_{HR}$  could result in an underestimation  
252 of the presence of euxinic conditions, and therefore  $(Fe_{ox} + Fe_{py})/Fe_{HR}$  is used to detect potential  $H_2S$   
253 accumulation on the seafloor. Consistently low  $(Fe_{ox} + Fe_{py})/Fe_{HR}$  values and elevated  $Fe_{HR}/Fe_T$  in this  
254 interval are indicative of ferruginous conditions (Poulton, 2021; Fig. 2). In the upper Fantasque  
255 Formation (10.0 to 14.3 m section height), pyrite framboids reappear and decrease in size up-section.  
256 Between 10 and 13 m, relatively large mean framboid diameters (6.8 to 9.6  $\mu m$ ) and modest trace metal  
257 enrichment suggest a return to predominantly dysoxic conditions. In the uppermost Fantasque Formation



258 (13.0 to 14.3 m), populations of smaller framboids (mean diameters 5.7 to 6.5  $\mu\text{m}$ ) and iron speciation  
259 results [ $\text{Fe}_{\text{HR}}/\text{Fe}_{\text{T}} < 0.38$ ;  $(\text{Fe}_{\text{ox}} + \text{Fe}_{\text{py}})/\text{Fe}_{\text{HR}} < 0.8$ ] point to fluctuating dysoxic to episodically anoxic,  
260 ferruginous conditions immediately preceding the P-T transition.

261 In the lower Grayling Formation of Ursula Creek, the majority of samples lack pyrite framboids,  
262 defining a short-lived Early Triassic "framboid gap", a phenomenon observed elsewhere and linked to  
263 ferruginous conditions or reoxygenation (e.g., Yang et al., 2024). At Ursula Creek, evaluated  $\text{Fe}_{\text{HR}}/\text{Fe}_{\text{T}}$   
264 values ( $> 0.38$ ) during this gap suggest the presence of anoxic conditions. While  $\text{Fe}_{\text{py}}$  concentrations are  
265 near zero,  $(\text{Fe}_{\text{ox}} + \text{Fe}_{\text{py}})/\text{Fe}_{\text{HR}}$  values are generally beyond 0.8. These iron data, combined with trace metal  
266 enrichments and  $\text{MO}_{\text{EF}}/\text{U}_{\text{EF}}$  values ranging from 0.1 to  $1.0 \times$  seawater, indicate that ferruginous conditions  
267 (oxygen-depleted and sulfide-free) prevailed in the earliest Triassic at Ursula Creek, punctuated by brief  
268 episodes of dysoxia (Fig. 2).

269 Previous work on the Chibi section has shown that the Upper Permian Talung Formation  
270 accumulated in predominantly dysoxic settings with intermittent anoxic/euxinic episodes, as indicated  
271 by abundant siliceous sponge spicules and radiolarians, rare calcareous benthic fossils, and pyrite  
272 framboid distributions (Yang et al., 2022; Fig. 5). Unlike at Ursula Creek, framboids at Chibi are well-  
273 preserved (Fig. 4C), negating concerns of significant oxidation after deposition and confirming the  
274 fidelity of the primary redox signals. Our new iron speciation data confirm this dynamic environment,  
275 with the latest Permian characterized by fluctuating euxinic (elevated  $\text{Fe}_{\text{HR}}/\text{Fe}_{\text{T}}$  and  $\text{Fe}_{\text{py}}/\text{Fe}_{\text{T}}$  values) and  
276 ferruginous (elevated  $\text{Fe}_{\text{HR}}/\text{Fe}_{\text{T}}$  but comparatively low  $\text{Fe}_{\text{py}}/\text{Fe}_{\text{T}}$  values) conditions (Fig. 5). Although the  
277 Lower Daye Formation (0 to 2.7 m section height) lacks pyrite framboids, other redox indicators  
278 including the presence of laminated, fossil-poor facies, carbonate Ce positive anomalies, evaluated  $\text{Fe}_{\text{HR}}$ ,  
279 and pyrite depletion collectively suggest the development of Fe(II)-rich, oxygen-depleted environments  
280 during the framboid gap interval (Yang et al., 2022; Müller et al., 2023; Fig. 5). The reoccurrence of  
281 populations of small framboids (mean diameters 5.6 to 7.2  $\mu\text{m}$ ) together with our iron speciation  
282 constraints, suggests that ferruginous settings persisted into the earliest Triassic, punctuated by  
283 intermittent dysoxic episodes (Yang et al., 2022; Fig. 5).

## 284 **5.2 P-T oceanic redox variation: causes and consequences**

285 To investigate global redox evolution across the P-T transition, we compiled iron speciation records from  
286 slope to basinal sections across Panthalassa, Tethys and the northwestern margin of Pangaea (Fig. 7). The



287 P-T transition in each section is defined by the initial occurrence of the conodont species *Hindeodus*  
288 *parvus* or, alternatively, the minimum value of the well-known first major P-T negative carbon isotopic  
289 excursion (e.g., Yuan et al., 2014; Yang et al., 2022).

290 The Waiheke section of New Zealand provides one of the few available records from Panthalassa.  
291 The elevated  $Fe_{HR}$  but low  $Fe_{py}$  and Mo/Al collectively suggest ferruginous conditions during the  
292 Changhsingian in this area (Grasby et al., 2021; Takahashi et al., 2021; Fig. 7). In bedded cherts of the  
293 P-T transition, high  $Fe_{HR}/Fe_T$  and U/Al ratios, coupled with strong pyritization and elevated Mo/Al values,  
294 indicate the presence of euxinic settings (Takahashi et al., 2021; Fig. 7). Two distinct intervals  
295 characterized by elevated  $Fe_{HR}/Fe_T$ , low  $Fe_{py}/Fe_{HR}$  and Mo/Al values are suggestive of recurring  
296 ferruginous episodes during the P-T transition. In contrast, low  $Fe_{HR}/Fe_T$  values ( $< 0.22$ ) during the  
297 earliest Triassic suggest episodes of reoxygenation (Takahashi et al., 2021; Fig. 7).

298 Stratigraphic records from the northern marginal slopes and basins of South China consistently  
299 document a transition from dysoxic/euxinic to ferruginous settings from the Late Permian to Early  
300 Triassic (Cao et al., 2009; Xiang et al., 2020; Yang et al., 2024). The Meishan GSSP section offers a  
301 particularly well-resolved example. There, evidence of green sulfur bacteria based on biomarkers  
302 suggests that euxinic conditions were widespread during the latest Permian (Cao et al., 2009). Several  
303 samples from the late Changhsingian part exhibit elevated  $Fe_{HR}/Fe_T$  ( $> 0.38$ ) and reduced  $Fe_{py}/Fe_{HR}$   
304 values ( $< 0.6$ ), indicating episodic ferruginous conditions (Xiang et al., 2020). In the earliest Triassic, a  
305 marked decline in  $Fe_{py}/Fe_{HR}$  values further supports stable ferruginous conditions at Meishan (Xiang et  
306 al., 2020; Fig. 7). This redox pattern is corroborated by iron speciation data from multiple well-  
307 documented sections including Ganxi, Xibeixiang, Chibi, Xiakou, Shangsi and Ruichang, which  
308 collectively support the development of regionally extensive ferruginous states in the earliest Triassic  
309 with episodic intervals of reoxygenation (Shen et al., 2016; Lei et al., 2017; Xiang et al., 2016; Ge et al.,  
310 2022; Yang et al., 2024; Fig. 7).

311 Iron speciation constraints from the Arabian Margin (Oman and the United Arab Emirates) in  
312 western Neo-Tethys, and from the Xiang-Qian-Gui Basin of South China, similarly point to iron-rich,  
313 oxygen-depleted marine environments prevailing from the end of the Permian into the earliest Triassic,  
314 interrupted by short-lived oxygenation pulses during the Changhsingian (Clarkson et al., 2016; Xiang et  
315 al., 2022; Yang et al., 2024).

316 The redox evolution along the northwestern margin of Pangaea exhibits significant spatial



317 heterogeneity. The Ursula Creek section records a transition from dysoxic conditions in the  
318 Changhsingian to ferruginous conditions in the Griesbachian. In contrast, sections in Spitsbergen  
319 (Festningen, Deltadalen) and Greenland (Fiskegrav) document an opposing trend: a shift from  
320 ferruginous conditions to euxinia (Bond and Wignall, 2010; Mettam et al., 2017; Schobben et al., 2020;  
321 Fig. 7).

322 These compiled records reveal a spatially heterogeneous and temporally dynamic global redox  
323 landscape across the P-T transition. During the latest Permian, ferruginous conditions intermittently  
324 developed across different ocean basins. In the earliest Triassic, however, ferruginous conditions  
325 expanded significantly, particularly within Tethys. This expansion may have been driven by a  
326 combination of processes: 1) extensive deposition of Late Permian evaporites and intensified anoxia  
327 accompanied by enhanced pyrite burial drew down the oceanic sulphate reservoir (Luo et al., 2010;  
328 Warren, 2010); 2) strong ocean stratification and sluggish circulation suppressed nutrient upwelling and  
329 marine primary productivity, thereby reducing organic-carbon fluxes and limiting microbial sulphate  
330 reduction (e.g., Song et al., 2014; Clarkson et al., 2016; Sun, 2024); and 3) intense weathering of Fe-  
331 bearing silicate minerals under the Early Triassic extreme greenhouse delivered abundant  $Fe_{HR}$  to the  
332 oceans, resulting in a marked rise in  $Fe_{HR}$  input over sulphate (e.g., Poulton and Canfield, 2011).

333 The widespread development of ferruginous conditions in early Triassic may have significantly  
334 impacted nutrient dynamics, with phosphorus (P) cycling being a key mediator—consistent with  
335 observations from past oceanic anoxic events (Papadomanolaki et al., 2022). Enhanced chemical  
336 weathering on land in the aftermath of the P-T transition likely boosted detrital delivery to the oceans  
337 (Sheldon, 2006; Algeo and Twitchett, 2010; Sun et al., 2018). However, despite the enhanced detrital  
338 delivery, marine primary productivity appears not to have risen over this period (e.g., Grasby et al., 2016,  
339 2020; Müller et al., 2022; Sun, 2024). This somewhat contradictory scenario could be attributed to strong  
340 thermal ocean stratification that inhibited upwelling and vertical mixing (Grasby et al., 2016; Knies et  
341 al., 2022). Additionally, the observed covariation between redox conditions and primary productivity  
342 across the P-T transition—where productivity was lower under ferruginous conditions and higher under  
343 euxinic conditions—suggests that the widespread ferruginous conditions in the Early Triassic likely  
344 imposed an additional constraint on primary production (e.g., Müller et al., 2022; Schobben et al., 2020;  
345 Ge et al., 2022; Woods et al., 2023). This productivity contrast may reflect differences in the  
346 bioavailability of P, whose biogeochemical behavior is strongly controlled by redox state. Euxinic



347 conditions enhance the P recycling through preferential organic matter preservation and suppressed  
348 authigenic apatite formation; this elevates bioavailable P fluxes, and stimulates productivity, which in  
349 turn maintains prolonged ocean deoxygenation (Ingall et al., 1993; Papadomanolaki et al., 2022). In  
350 contrast, ferruginous environments could have inhibited the recycling of bioavailable P through  
351 precipitation of Fe(II)-bearing phosphates (e.g., vivianite), incorporation into green-rust phases, and co-  
352 precipitation with iron oxides (Bjerrum and Canfield, 2002; Zegeye et al., 2012; Xiong et al., 2019),  
353 although direct mineralogical evidence for ferrous phosphates has not yet been identified from the P-T  
354 interval. Therefore, oxygen depletion, together with the potential linkage between ferruginous conditions  
355 and nutrient limitation, may have been instrumental in triggering the EPME and delaying the recovery.

## 356 **6 Conclusions**

357 Permian-Triassic records from equatorial eastern Tethys (Chibi, South China) and the northwestern  
358 margin of Pangaea (Ursula Creek, western Canada) record redox evolution across this major transition  
359 in Earth history. A multi-proxy approach combining pyrite framboid size distributions, iron speciation  
360 results, and Mo-U covariation suggests that predominantly dysoxic bottom waters that were established  
361 during the latest Permian in each of these palaeogeographically distinct locations gave way to intense  
362 anoxia near the EPME horizon. In the earliest Triassic, the absence of pyrite framboids, coupled with  
363 iron proxies and other redox proxies (Ce-anomalies and Mo-U covariation), points to an expansion of  
364 ferruginous conditions in epicontinental settings. The shift from dysoxic to ferruginous conditions  
365 implies that the EPME was triggered by oxygen and nutrient limitation under ferruginous anoxia.

## 366 **Author contributions**

367 All authors have been involved in the present work, have approved the manuscript, and agree to its  
368 submission. Fen Yang designed this study. Fen Yang, Yadong Sun, Stephen E. Grasby and David P.G.  
369 Bond collected the samples used in this study. Fen Yang completed the data preparation and analysis with  
370 the help of Sen Li. The manuscript was mainly written by Fen Yang and Sen Li with contributions from  
371 all authors. Sen Li is designated as the main corresponding author: [lisen@cug.edu.cn](mailto:lisen@cug.edu.cn).

## 372 **Competing interests**



373 The authors confirm that there are no financial or personal affiliations that could be perceived as  
374 influencing the results presented in this study.

#### 375 **Financial support**

376 This work was jointly supported by the National Natural Science Foundation of China (Grant No.  
377 42272022), the China Postdoctoral Science Foundation (grants No. 2025M770406), the geological  
378 survey projects of the China Geological Survey (Grants DD202501029, DD20242650). DPGB  
379 acknowledges NERC Grant NE/V001639/1.

#### 380 **References**

- 381 Alcott, L. J., Krause, A. J., Hammarlund, E. U., Bjerrum, C. J., Scholz, F., Xiong, Y., Hobson, A. J., Neve,  
382 L., Mills, B. J. W., März, C., Schnetger, B., Bekker, A., and Poulton, S. W.: Development of Iron  
383 Speciation Reference Materials for Palaeoredox Analysis, *Geostand. Geoanal. Res.*, 44, 581–591,  
384 <https://doi.org/10.1111/ggr.12342>, 2020.
- 385 Algeo, T. J. and Ingall, E.: Sedimentary Corg:P ratios, paleocean ventilation, and Phanerozoic  
386 atmospheric  $pO_2$ , *Palaeogeogr. Palaeoclimatol. Palaeoecol.*, 256, 130–155,  
387 <https://doi.org/10.1016/j.palaeo.2007.02.029>, 2007.
- 388 Algeo, T. J. and Li, C.: Redox classification and calibration of redox thresholds in sedimentary systems,  
389 *Geochim. Cosmochim. Acta.*, 287, 8–26, <https://doi.org/10.1016/j.gca.2020.01.055>, 2020.
- 390 Algeo, T. J. and Tribouillard, N.: Environmental analysis of paleoceanographic systems based on  
391 molybdenum–uranium covariation, *Chem. Geol.*, 268, 211–225,  
392 <https://doi.org/10.1016/j.chemgeo.2009.09.001>, 2009.
- 393 Algeo, T. J. and Twitchett, R. J.: Anomalous Early Triassic sediment fluxes due to elevated weathering  
394 rates and their biological consequences, *Geology*, 38, 1023–1026, <https://doi.org/10.1130/G31203.1>,  
395 2010.
- 396 Algeo, T. J., Hinnov, L., Moser, J., Maynard, J. B., Elswick, E., Kuwahara, K., and Sano, H.: Changes in  
397 productivity and redox conditions in the Panthalassic Ocean during the latest Permian, *Geology*, 38, 187–  
398 190, <https://doi.org/10.1130/G30483.1>, 2010.
- 399 Beatty, T. W., Zonneveld, J. P., and Henderson, C. M.: Anomalously diverse Early Triassic ichnofossil



- 400 assemblages in northwest Pangea: A case for a shallow-marine habitable zone, *Geology*, 36, 771–774,  
401 <https://doi.org/10.1130/G24952A.1>, 2008.
- 402 Bjerrum, C. J. and Canfield, D. E.: Ocean productivity before about 1.9 Gyr ago limited by phosphorus  
403 adsorption onto iron oxides, *Nature*, 417, 159–162, <https://doi.org/10.1038/417159a>, 2002.
- 404 Bond, D. P. G. and Wignall, P. B.: Pyrite framboid study of marine Permian–Triassic boundary sections:  
405 A complex anoxic event and its relationship to contemporaneous mass extinction, *GSA Bulletin.*, 122,  
406 1265–1279, <https://doi.org/10.1130/B30042.1>, 2010.
- 407 Canfield, D. E., Raiswell, R., Westrich, J. T., Reaves, C. M., and Berner, R. A.: The use of chromium  
408 reduction in the analysis of reduced inorganic sulfur in sediments and shales, *Chem. Geol.*, 54, 149–155,  
409 [https://doi.org/10.1016/0009-2541\(86\)90078-1](https://doi.org/10.1016/0009-2541(86)90078-1), 1986.
- 410 Canfield, D. E., Poulton, S. W., Knoll, A. H., Narbonne, G. M., Ross, G., Goldberg, T., and Strauss, H.:  
411 Ferruginous Conditions Dominated Later Neoproterozoic Deep-Water Chemistry, *Science*, 321, 949–952,  
412 <https://doi.org/10.1126/science.1154499>, 2008.
- 413 Cao, C., Love, G. D., Hays, L. E., Wang, W., Shen, S., and Summons, R. E.: Biogeochemical evidence  
414 for euxinic oceans and ecological disturbance presaging the end-Permian mass extinction event, *Earth  
415 Planet. Sci. Lett.*, 281, 188–201, <https://doi.org/10.1016/j.epsl.2009.02.012>, 2009.
- 416 Chen, Z. Q. and Benton, M. J.: The timing and pattern of biotic recovery following the end-Permian mass  
417 extinction, *Nature Geosci.*, 5, 375–383, <https://doi.org/10.1038/ngeo1475>, 2012.
- 418 Chen, Z. Q., Fang, Y., Wignall, P. B., Guo, Z., Wu, S., Liu, Z., Wang, R., Huang, Y., and Feng, X.:  
419 Microbial Blooms Triggered Pyrite Framboid Enrichment and Oxygen Depletion in Carbonate Platforms  
420 Immediately After the Latest Permian Extinction, *Geophys. Res. Lett.*, 49, e2021GL096998,  
421 <https://doi.org/10.1029/2021GL096998>, 2022.
- 422 Clarkson, M. O., Poulton, S. W., Guilbaud, R., and Wood, R. A.: Assessing the utility of Fe/Al and Fe-  
423 speciation to record water column redox conditions in carbonate-rich sediments, *Chem. Geol.*, 382, 111–  
424 122, <https://doi.org/10.1016/j.chemgeo.2014.05.031>, 2014.
- 425 Clarkson, M. O., Wood, R. A., Poulton, S. W., Richoz, S., Newton, R. J., Kasemann, S. A., Bowyer, F.,  
426 and Krystyn, L.: Dynamic anoxic ferruginous conditions during the end-Permian mass extinction and  
427 recovery, *Nat Commun.*, 7, 12236, <https://doi.org/10.1038/ncomms12236>, 2016.
- 428 Derry, L. A.: Causes and consequences of mid-Proterozoic anoxia, *Geophys. Res. Lett.*, 42, 8538–8546,  
429 <https://doi.org/10.1002/2015GL065333>, 2015.



- 430 Erwin, D. H.: Extinction: How life on Earth nearly ended 250 million years ago, Princeton University  
431 Press, Princeton, NJ, US, viii, 296 pp., 2006.
- 432 Feng, Z. Z., Yang, Y. Q., Jin, Z. K., He, Y. B., Wu, S. H., Xin, W. J., Bao, Z. D., and Tan, J.: Lithofacies  
433 paleogeography of the Permian of South China. *Acta Sedimentol. Sin.* 14 (2), 1–11, 1996 (in Chinese  
434 with English abstract).
- 435 Foster, W. J. and Twitchett, R. J.: Functional diversity of marine ecosystems after the Late Permian mass  
436 extinction event, *Nature Geosci.*, 7, 233–238, <https://doi.org/10.1038/ngeo2079>, 2014.
- 437 Frank, A. B., Karapınar, B., Grasby, S. E., Koşun, E., Lahajnar, N., Gómez Correa, M. A., Buchwald, S.  
438 Z., Metzke, M., and Foster, W. J.: Assessing the role of anoxia as a potential extinction driver in the  
439 shallow marine Neotethys during the Permian-Triassic mass extinction, *Chem. Geol.*, 696, 123108,  
440 <https://doi.org/10.1016/j.chemgeo.2025.123108>, 2025.
- 441 Garbelli, C., Angiolini, L., Brand, U., Shen, S., Jadoul, F., Posenato, R., Azmy, K., and Cao, C.: Neotethys  
442 seawater chemistry and temperature at the dawn of the end Permian mass extinction, *Gondwana Res.*,  
443 35, 272–285, <https://doi.org/10.1016/j.gr.2015.05.012>, 2016.
- 444 Ge, X., Chen, D., Zhang, G., Huang, T., Liu, M., and El-Shafei, M.: Marine redox evolution and organic  
445 accumulation in an intrashelf basin, NE Sichuan Basin during the Late Permian, *Mar. Pet. Geol.*, 140,  
446 105633, <https://doi.org/10.1016/j.marpetgeo.2022.105633>, 2022.
- 447 Ge, Y. and Bond, D. P. G.: Two deep marine oxygenation events during the Permian-Triassic boundary  
448 interval in South China: Relationship with ocean circulation and marine primary productivity, *Earth-sci.*  
449 *Rev.*, 234, 104220, <https://doi.org/10.1016/j.earscirev.2022.104220>, 2022.
- 450 Georgiev, S. V., Horner, T. J., Stein, H. J., Hannah, J. L., Bingen, B., and Rehkämper, M.: Cadmium-  
451 isotopic evidence for increasing primary productivity during the Late Permian anoxic event, *Earth Planet.*  
452 *Sci. Lett.*, 410, 84–96, <https://doi.org/10.1016/j.epsl.2014.11.010>, 2015.
- 453 Grasby, S. E. and Beauchamp, B.: Intra-basin variability of the carbon-isotope record across the Permian–  
454 Triassic transition, Sverdrup Basin, Arctic Canada, *Chem. Geol.*, 253, 141–150,  
455 <https://doi.org/10.1016/j.chemgeo.2008.05.005>, 2008.
- 456 Grasby, S. E., Beauchamp, B., Embry, A., and Sanei, H.: Recurrent Early Triassic ocean anoxia, *Geology*,  
457 41, 175–178, <https://doi.org/10.1130/G33599.1>, 2013.
- 458 Grasby, S. E., Beauchamp, B., and Knies, J.: Early Triassic productivity crises delayed recovery from  
459 world’s worst mass extinction, *Geology*, 44, 779–782, <https://doi.org/10.1130/G38141.1>, 2016.



- 460 Grasby, S. E., Knies, J., Beauchamp, B., Bond, D. P. G., Wignall, P., and Sun, Y.: Global warming leads  
461 to Early Triassic nutrient stress across northern Pangea, *GSA Bulletin.*, 132, 943–954,  
462 <https://doi.org/10.1130/B32036.1>, 2019.
- 463 Grasby, S. E., Bond, D. P. G., Wignall, P. B., Yin, R., Strachan, L. J., and Takahashi, S.: Transient  
464 Permian-Triassic euxinia in the southern Panthalassa deep ocean, *Geology*, 49, 889–893,  
465 <https://doi.org/10.1130/G48928.1>, 2021.
- 466 Grice, K., Cao, C., Love, G. D., Böttcher, M. E., Twitchett, R. J., Grosjean, E., Summons, R. E., Turgeon,  
467 S. C., Dunning, W., and Jin, Y.: Photic Zone Euxinia During the Permian-Triassic Superanoxic Event,  
468 *Science*, 307, 706–709, <https://doi.org/10.1126/science.1104323>, 2005.
- 469 Henderson, C. M.: Uppermost Permian conodonts and the Permian-Triassic boundary in the Western  
470 Canada Sedimentary Basin, *Bulletin of Canadian Petroleum Geology*, 45, 693–707,  
471 <https://doi.org/10.35767/gscpgbull.45.4.693>, 1997.
- 472 Hotinski, R. M., Bice, K. L., Kump, L. R., Najjar, R. G., and Arthur, M. A.: Ocean stagnation and end-  
473 Permian anoxia, *Geology*, 29, 7–10, [https://doi.org/10.1130/0091-7613\(2001\)029<0007:OSAEPA>2.0.CO;2](https://doi.org/10.1130/0091-7613(2001)029<0007:OSAEPA>2.0.CO;2), 2001.
- 475 Ingall, E. D., Bustin, R. M., and Van Cappellen, P.: Influence of water column anoxia on the burial and  
476 preservation of carbon and phosphorus in marine shales, *Geochim. Cosmochim. Acta.*, 57, 303–316,  
477 [https://doi.org/10.1016/0016-7037\(93\)90433-W](https://doi.org/10.1016/0016-7037(93)90433-W), 1993.
- 478 Isozaki, Y.: Permo-Triassic Boundary Superanoxia and Stratified Superocean: Records from Lost Deep  
479 Sea, *Science*, 276, 235–238, <https://doi.org/10.1126/science.276.5310.235>, 1997.
- 480 Joachimski, M. M., Lai, X., Shen, S., Jiang, H., Luo, G., Chen, B., Chen, J., and Sun, Y.: Climate warming  
481 in the latest Permian and the Permian–Triassic mass extinction, *Geology*, 40, 195–198,  
482 <https://doi.org/10.1130/G32707.1>, 2012.
- 483 Knies, J., Schönenberger, J., Zwingmann, H., van der Lelij, R., Smelror, M., Vullum, P. E., Brönnner, M.,  
484 Vogt, C., Fredin, O., Müller, A., Grasby, S. E., Beauchamp, B., and Viola, G.: Continental weathering  
485 and recovery from ocean nutrient stress during the Early Triassic Biotic Crisis, *Commun Earth Environ.*,  
486 3, 161, <https://doi.org/10.1038/s43247-022-00480-z>, 2022.
- 487 Knoll, A. H., Bambach, R. K., Canfield, D. E., and Grotzinger, J. P.: Comparative Earth History and Late  
488 Permian Mass Extinction, *Science*, 273, 452–457, <https://doi.org/10.1126/science.273.5274.452>, 1996.
- 489 Kump, L. R., Pavlov, A., and Arthur, M. A.: Massive release of hydrogen sulfide to the surface ocean and



- 490 atmosphere during intervals of oceanic anoxia, *Geology*, 33, 397–400, <https://doi.org/10.1130/G21295.1>,  
491 2005.
- 492 Lau, K. V., Maher, K., Altiner, D., Kelley, B. M., Kump, L. R., Lehrmann, D. J., Silva-Tamayo, J. C.,  
493 Weaver, K. L., Yu, M., and Payne, J. L.: Marine anoxia and delayed Earth system recovery after the end-  
494 Permian extinction, *Proc. Natl. Acad. Sci.*, 113, 2360–2365, <https://doi.org/10.1073/pnas.1515080113>,  
495 2016.
- 496 Lei, L. D., Shen, J., Li, C., Algeo, T. J., Chen, Z. Q., Feng, Q. L., Cheng, M., Jin, C. S., and Huang, J. H.:  
497 Controls on regional marine redox evolution during Permian-Triassic transition in South China,  
498 *Palaeogeogr. Palaeoclimatol. Palaeoecol.*, 486, 17–32, <https://doi.org/10.1016/j.palaeo.2017.02.010>,  
499 2017.
- 500 Luo, G., Kump, L. R., Wang, Y., Tong, J., Arthur, M. A., Yang, H., Huang, J., Yin, H., and Xie, S.: Isotopic  
501 evidence for an anomalously low oceanic sulfate concentration following end-Permian mass extinction,  
502 *Earth Planet. Sci. Lett.*, 300, 101–111, <https://doi.org/10.1016/j.epsl.2010.09.041>, 2010.
- 503 Luo, G., Wang, Y., Grice, K., Kershaw, S., Algeo, T. J., Ruan, X., Yang, H., Jia, C., and Xie, S.:  
504 Microbial–algal community changes during the latest Permian ecological crisis: Evidence from lipid  
505 biomarkers at Cili, South China, *Glob. Planet. Change.*, 105, 36–51,  
506 <https://doi.org/10.1016/j.gloplacha.2012.11.015>, 2013.
- 507 Mettam, C., Zerkle, A. L., Claire, M. W., Izon, G., Junium, C. J., and Twitchett, R. J.: High-frequency  
508 fluctuations in redox conditions during the latest Permian mass extinction, *Paleogeogr. Paleoclimatol.*  
509 *Paleoecol.*, 485, 210–223, <https://doi.org/10.1016/j.palaeo.2017.06.014>, 2017.
- 510 Meyer, K. M., Kump, L. R., and Ridgwell, A.: Biogeochemical controls on photic-zone euxinia during  
511 the end-Permian mass extinction, *Geology*, 36, 747–750, <https://doi.org/10.1130/G24618A.1>, 2008.
- 512 Müller, J., Sun, Y., Yang, F., Fantasia, A., and Joachimski, M.: Phosphorus Cycle and Primary  
513 Productivity Changes in the Tethys Ocean During the Permian-Triassic Transition: Starving Marine  
514 Ecosystems, *Front. Earth Sci.*, 10, <https://doi.org/10.3389/feart.2022.832308>, 2022.
- 515 Müller, J., Sun, Y. D., Yang, F., Regelous, M., and Joachimski, M. M.: Manganous water column in the  
516 Tethys Ocean during the Permian-Triassic transition, *Glob. Planet. Change.*, 222, 104067,  
517 <https://doi.org/10.1016/j.gloplacha.2023.104067>, 2023.
- 518 Newby, S. M., Owens, J. D., Schoepfer, S. D., and Algeo, T. J.: Transient ocean oxygenation at end-  
519 Permian mass extinction onset shown by thallium isotopes, *Nat. Geosci.*, 14, 678–683,



- 520 <https://doi.org/10.1038/s41561-021-00802-4>, 2021.
- 521 Nielsen, J. K., Shen, Y., Piasecki, S., and Stemmerik, L.: No abrupt change in redox condition caused the  
522 end-Permian marine ecosystem collapse in the East Greenland Basin, *Earth Planet. Sci. Lett.*, 291, 32–  
523 38, <https://doi.org/10.1016/j.epsl.2009.12.043>, 2010.
- 524 Papadomanolaki, N. M., Lenstra, W. K., Wolthers, M., and Slomp, C. P.: Enhanced phosphorus recycling  
525 during past oceanic anoxia amplified by low rates of apatite authigenesis, *Sci. Adv.*, 8, eabn2370,  
526 <https://doi.org/10.1126/sciadv.abn2370>, 2022.
- 527 Poulton, S. W.: The low-temperature geochemical cycle of iron: From continental fluxes to marine  
528 sediment deposition, *Am. J. Sci.*, 302, 774–805, <https://doi.org/10.2475/ajs.302.9.774>, 2002.
- 529 Poulton, S. W.: The Iron Speciation Paleoredox Proxy, *Elements in Geochemical Tracers in Earth System*  
530 *Science*, <https://doi.org/10.1017/9781108847148>, 2021.
- 531 Poulton, S. W. and Canfield, D. E.: Development of a sequential extraction procedure for iron:  
532 implications for iron partitioning in continentally derived particulates, *Chem. Geol.*, 214, 209–221,  
533 <https://doi.org/10.1016/j.chemgeo.2004.09.003>, 2005.
- 534 Poulton, S. W. and Canfield, D. E.: Ferruginous Conditions: A Dominant Feature of the Ocean through  
535 Earth's History, *Elements*, 7, 107–112, <https://doi.org/10.2113/gselements.7.2.107>, 2011.
- 536 Proemse, B. C., Grasby, S. E., Wieser, M. E., Mayer, B., and Beauchamp, B.: Molybdenum isotopic  
537 evidence for oxic marine conditions during the latest Permian extinction, *Geology*, 41, 967–970,  
538 <https://doi.org/10.1130/G34466.1>, 2013.
- 539 Pruss, S. B., Bottjer, D. J., Corsetti, F. A., and Baud, A.: A global marine sedimentary response to the  
540 end-Permian mass extinction: Examples from southern Turkey and the western United States, *Earth-sci.*  
541 *Rev.*, 78, 193–206, <https://doi.org/10.1016/j.earscirev.2006.05.002>, 2006.
- 542 Schobben, M., Foster, W. J., Sleveland, A. R. N., Zuchuat, V., Svensen, H. H., Planke, S., Bond, D. P. G.,  
543 Marcelis, F., Newton, R. J., Wignall, P. B., and Poulton, S. W.: A nutrient control on marine anoxia during  
544 the end-Permian mass extinction, *Nat. Geosci.*, 13, 640–646, [https://doi.org/10.1038/s41561-020-0622-](https://doi.org/10.1038/s41561-020-0622-1)  
545 1, 2020.
- 546 Schoepfer, S. D., Henderson, C. M., Garrison, G. H., Foriel, J., Ward, P. D., Selby, D., Hower, J. C.,  
547 Algeo, T. J. and Shen, Y.: Termination of a continent-margin upwelling system at the Permian–Triassic  
548 boundary (Opal Creek, Alberta, Canada), *Glob. Planet. Change.*, 105, 21–35,  
549 <https://doi.org/10.1016/j.gloplacha.2012.07.005>, 2013.



- 550 Scholz, F., McManus, J., and Sommer, S.: The manganese and iron shuttle in a modern euxinic basin and  
551 implications for molybdenum cycling at euxinic ocean margins, *Chem. Geol.*, 355, 56–68,  
552 <https://doi.org/10.1016/j.chemgeo.2013.07.006>, 2013.
- 553 Scotese, C.: Atlas of Middle & Late Permian and Triassic Paleogeographic Maps, Scotese, C.R., 2014.  
554 Atlas of Middle & Late Permian and Triassic Paleogeographic Maps, Maps 43–52, Volumes 3 & 4,  
555 PALEOMAP PaleoAtlas for ArcGIS, PALEOMAP Project, Evanston, IL., 2014.
- 556 Sepkoski, J. J.: A Factor Analytic Description of the Phanerozoic Marine Fossil Record, *Paleobiology*, 7,  
557 36–53, 1981.
- 558 Sheldon, N. D.: Abrupt chemical weathering increase across the Permian–Triassic boundary, *Palaeogeogr.*  
559 *Palaeoclimatol. Palaeoecol.*, 231, 315–321, <https://doi.org/10.1016/j.palaeo.2005.09.001>, 2006.
- 560 Shen, J., Algeo, T. J., Hu, Q., Zhang, N., Zhou, L., Xia, W., Xie, S., and Feng, Q.: Negative C-isotope  
561 excursions at the Permian-Triassic boundary linked to volcanism, *Geology*, 40, 963–966,  
562 <https://doi.org/10.1130/G33329.1>, 2012.
- 563 Shen, J., Feng, Q., Algeo, T. J., Li, C., Planavsky, N. J., Zhou, L., and Zhang, M.: Two pulses of oceanic  
564 environmental disturbance during the Permian–Triassic boundary crisis, *Earth Planet. Sci. Lett.*, 443,  
565 139–152, <https://doi.org/10.1016/j.epsl.2016.03.030>, 2016.
- 566 Shen, Y., Farquhar, J., Zhang, H., Masterson, A., Zhang, T., and Wing, B. A.: Multiple S-isotopic evidence  
567 for episodic shoaling of anoxic water during Late Permian mass extinction, *Nat Commun.*, 2, 210,  
568 <https://doi.org/10.1038/ncomms1217>, 2011.
- 569 Song, H., Tong, J., Algeo, T. J., Song, H., Qiu, H., Zhu, Y., Tian, L., Bates, S., Lyons, T. W., Luo, G., and  
570 Kump, L. R.: Early Triassic seawater sulfate drawdown, *Geochim. Cosmochim. Acta.*, 128, 95–113,  
571 <https://doi.org/10.1016/j.gca.2013.12.009>, 2014.
- 572 Sperling, E. A., Wolock, C. J., Morgan, A. S., Gill, B. C., Kunzmann, M., Halverson, G. P., Macdonald,  
573 F. A., Knoll, A. H., and Johnston, D. T.: Statistical analysis of iron geochemical data suggests limited late  
574 Proterozoic oxygenation, *Nature*, 523, 451–454, <https://doi.org/10.1038/nature14589>, 2015.
- 575 Stebbins, A., Williams, J., Brookfield, M., Nye, S. W., and Hannigan, R.: Frequent euxinia in southern  
576 Neo-Tethys Ocean prior to the end-Permian biocrisis: Evidence from the Spiti region, India, *Palaeogeogr.*  
577 *Palaeoclimatol. Palaeoecol.*, 516, 1–10, <https://doi.org/10.1016/j.palaeo.2018.11.030>, 2019.
- 578 Sun, H., Xiao, Y., Gao, Y., Zhang, G., Casey, J. F., and Shen, Y.: Rapid enhancement of chemical  
579 weathering recorded by extremely light seawater lithium isotopes at the Permian–Triassic boundary, *Proc.*



- 580 Natl. Acad. Sci., 115, 3782–3787, <https://doi.org/10.1073/pnas.1711862115>, 2018.
- 581 Sun, Y.: Dynamics of nutrient cycles in the Permian–Triassic oceans, *Earth-Sci. Rev.*, 258, 104914,  
582 <https://doi.org/10.1016/j.earscirev.2024.104914>, 2024.
- 583 Sun, Y., Joachimski, M. M., Wignall, P. B., Yan, C., Chen, Y., Jiang, H., Wang, L., and Lai, X.: Lethally  
584 Hot Temperatures During the Early Triassic Greenhouse, *Science*, 338, 366–370,  
585 <https://doi.org/10.1126/science.1224126>, 2012.
- 586 Takahashi, S., Oba, M., Kaiho, K., Yamakita, S., and Sakata, S.: Panthalassic oceanic anoxia at the end  
587 of the Early Triassic: A cause of delay in the recovery of life after the end-Permian mass extinction,  
588 *Palaeogeogr. Palaeoclimatol. Palaeoecol.*, 274, 185–195, <https://doi.org/10.1016/j.palaeo.2009.01.010>,  
589 2009.
- 590 Takahashi, S., Hori, R. S., Yamakita, S., Aita, Y., Takemura, A., Ikehara, M., Xiong, Y., Poulton, S. W.,  
591 Wignall, P. B., Itai, T., Campbell, H. J., and Spörl, B. K.: Progressive development of ocean anoxia in  
592 the end-Permian pelagic Panthalassa, *Glob. Planet. Change.*, 207, 103650,  
593 <https://doi.org/10.1016/j.gloplacha.2021.103650>, 2021.
- 594 Taniwaki, T., Elders, C., Böttcher, M. E., Holman, A. I., and Grice, K.: Photic zone redox oscillations  
595 and microbialite development recorded by Early Triassic sediments of the Perth Basin: A geochemical  
596 approach, *Geochim. Cosmochim. Acta.*, 336, 188–207, <https://doi.org/10.1016/j.gca.2022.09.011>, 2022.
- 597 Taylor, S. and McLennan, S.: *The Continental Crust: Its Composition and Evolution*, Department of  
598 Geosciences Faculty Publications, 1985.
- 599 Tribouillard, N., Algeo, T. J., Lyons, T., and Riboulleau, A.: Trace metals as paleoredox and  
600 paleoproductivity proxies: An update, *Chem. Geol.*, 232, 12–32,  
601 <https://doi.org/10.1016/j.chemgeo.2006.02.012>, 2006.
- 602 Tribouillard, N., Algeo, T. J., Baudin, F., and Riboulleau, A.: Analysis of marine environmental  
603 conditions based on molybdenum–uranium covariation—Applications to Mesozoic paleoceanography,  
604 *Chem. Geol.*, 324–325, 46–58, <https://doi.org/10.1016/j.chemgeo.2011.09.009>, 2012.
- 605 Warren, J. K.: Evaporites through time: Tectonic, climatic and eustatic controls in marine and nonmarine  
606 deposits, *Earth Sci. Rev.*, 98, 217–268, <https://doi.org/10.1016/j.earscirev.2009.11.004>, 2010.
- 607 Wignall, P. and Twitchett, R.: Extent, duration, and nature of the Permian-Triassic superanoxic event, in:  
608 *Catastrophic events and mass extinctions: impacts and beyond*, vol. Special Paper 356, edited by:  
609 Koeberl, C. and MacLeod, K., Geological Society of America, 395–413, 2002.



- 610 Wignall, P. B. and Hallam, A.: Anoxia as a cause of the Permian/Triassic mass extinction: facies evidence  
611 from northern Italy and the western United States, *Palaeogeogr. Palaeoclimatol. Palaeoecol.*, 93, 21–46,  
612 [https://doi.org/10.1016/0031-0182\(92\)90182-5](https://doi.org/10.1016/0031-0182(92)90182-5), 1992.
- 613 Wignall, P. B. and Newton, R.: Contrasting Deep-Water Records from the Upper Permian and Lower  
614 Triassic of South Tibet and British Columbia: Evidence for a Diachronous Mass Extinction, *Palaios*, 18,  
615 153–167, 2003.
- 616 Wignall, P. B. and Twitchett, R. J.: Oceanic Anoxia and the End Permian Mass Extinction, *Science*, 272,  
617 1155–1158, <https://doi.org/10.1126/science.272.5265.1155>, 1996.
- 618 Wilkin, R. T. and Barnes, H. L.: Pyrite formation by reactions of iron monosulfides with dissolved  
619 inorganic and organic sulfur species, *Geochim. Cosmochim. Acta.*, 60, 4167–4179,  
620 [https://doi.org/10.1016/S0016-7037\(97\)81466-4](https://doi.org/10.1016/S0016-7037(97)81466-4), 1996.
- 621 Wilkin, R. T., Barnes, H. L., and Brantley, S. L.: The size distribution of framboidal pyrite in modern  
622 sediments: An indicator of redox conditions, *Geochim. Cosmochim. Acta.*, 60, 3897–3912,  
623 [https://doi.org/10.1016/0016-7037\(96\)00209-8](https://doi.org/10.1016/0016-7037(96)00209-8), 1996.
- 624 Woods, A. D., Zonneveld, J. P., and Wakefield, R.: Hyperthermal-driven anoxia and reduced productivity  
625 in the aftermath of the Permian-Triassic mass extinction: a case study from Western Canada, *Front. Earth  
626 Sci.*, 11, <https://doi.org/10.3389/feart.2023.1323413>, 2023.
- 627 Xiang, L., Schoepfer, S. D., Zhang, H., Yuan, D., Cao, C., Zheng, Q., Henderson, C. M., and Shen, S.:  
628 Oceanic redox evolution across the end-Permian mass extinction at Shangsi, South China, *Paleogeogr.  
629 Paleoclimatol. Paleoecol.* 448, 59–71, <https://doi.org/10.1016/j.palaeo.2015.10.046>, 2016.
- 630 Xiang, L., Zhang, H., Schoepfer, S. D., Cao, C., Zheng, Q., Yuan, D., Cai, Y., and Shen, S.: Oceanic  
631 redox evolution around the end-Permian mass extinction at Meishan, South China, *Paleogeogr.  
632 Paleoclimatol. Paleoecol.*, 544, 109626, <https://doi.org/10.1016/j.palaeo.2020.109626>, 2020.
- 633 Xiang, L., Schoepfer, S. D., Yuan, D. X., Zheng, Q. F., and Zhang, H.: Oceanic redox evolution across  
634 the end-Permian mass extinction at Penglaitan section, South China, *Palaeoworld*, 31, 93–102,  
635 <https://doi.org/10.1016/j.palwor.2021.02.003>, 2022.
- 636 Xiong, Y., Guilbaud, R., Peacock, C. L., Cox, R. P., Canfield, D. E., Krom, M. D., and Poulton, S. W.:  
637 Phosphorus cycling in Lake Cadagno, Switzerland: A low sulfate euxinic ocean analogue, *Geochim.  
638 Cosmochim. Acta.*, 251, 116–135, <https://doi.org/10.1016/j.gca.2019.02.011>, 2019.
- 639 Yang, F., Sun, Y. D., Frings, P. J., Luo, L., E, J. W., Wang, L. N., Huang, Y. F., Wang, T., Müller, J., and



- 640 Xie, S. C.: Collapse of Late Permian chert factories in the equatorial Tethys and the nature of the Early  
641 Triassic chert gap, *Earth Planet. Sci. Lett.*, 600, 117861, <https://doi.org/10.1016/j.epsl.2022.117861>, 2022.
- 642 Yang, F., Li, S., An, K.Y., Bond, P.G.D., Ao, R., Wu, X.B., Ma, L.L., and Sun, Y.D.: 2024. Re-Evaluating  
643 Water Column Reoxygenation During the End Permian Mass Extinction. *Geochem. Geophys. Geosyst.*  
644 25, <https://doi.org/10.1029/2024gc011779>, 2024.
- 645 Yuan, D., Shen, S., Henderson, C. M., Chen, J., Zhang, H., and Feng, H.: Revised conodont-based  
646 integrated high-resolution timescale for the Changhsingian Stage and end-Permian extinction interval at  
647 the Meishan sections, South China, *Lithos*, 204, 220–245, <https://doi.org/10.1016/j.lithos.2014.03.026>,  
648 2014.
- 649 Zegeye, A., Bonneville, S., Benning, L. G., Sturm, A., Fowle, D. A., Jones, C., Canfield, D. E., Ruby, C.,  
650 MacLean, L. C., Nomosatryo, S., Crowe, S. A., and Poulton, S. W.: Green rust formation controls nutrient  
651 availability in a ferruginous water column, *Geology*, 40, 599–602, <https://doi.org/10.1130/G32959.1>,  
652 2012.
- 653 Zhang, G., Zhang, X., Hu, D., Li, D., Algeo, T. J., Farquhar, J., Henderson, C. M., Qin, L., Shen, M.,  
654 Shen, D., Schoepfer, S. D., Chen, K., and Shen, Y.: Redox chemistry changes in the Panthalassic Ocean  
655 linked to the end-Permian mass extinction and delayed Early Triassic biotic recovery, *Proc. Natl. Acad.*  
656 *Sci. U.S.A.*, 114, 1806–1810, <https://doi.org/10.1073/pnas.1610931114>, 2017.

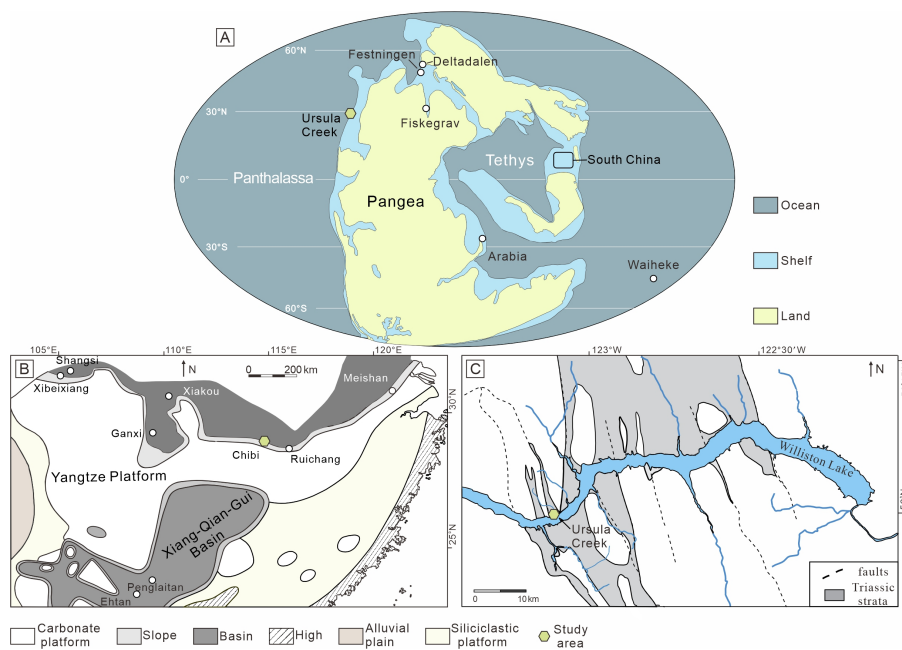
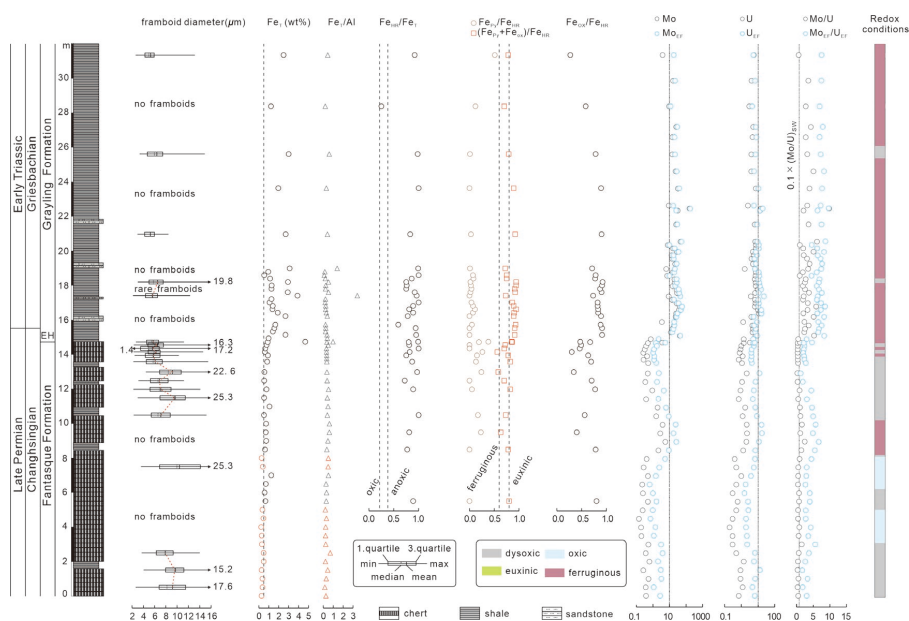
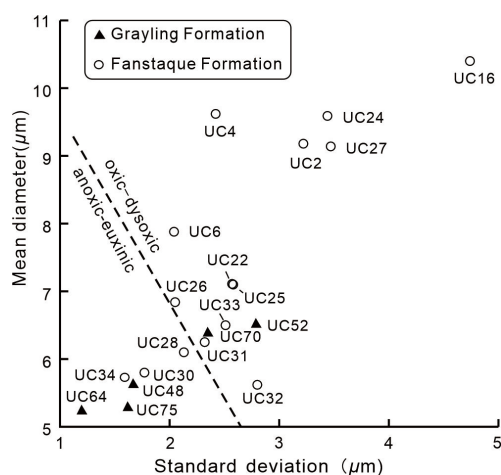


Figure 1. (A) Palaeogeographic reconstruction of Pangaea in the Late Permian (modified from Scotese, 2014). (B) Palaeogeographic reconstruction of the South China Block during the Changhsingian (modified from Feng et al., 1996). (C) Locations of the Ursula Creek section.



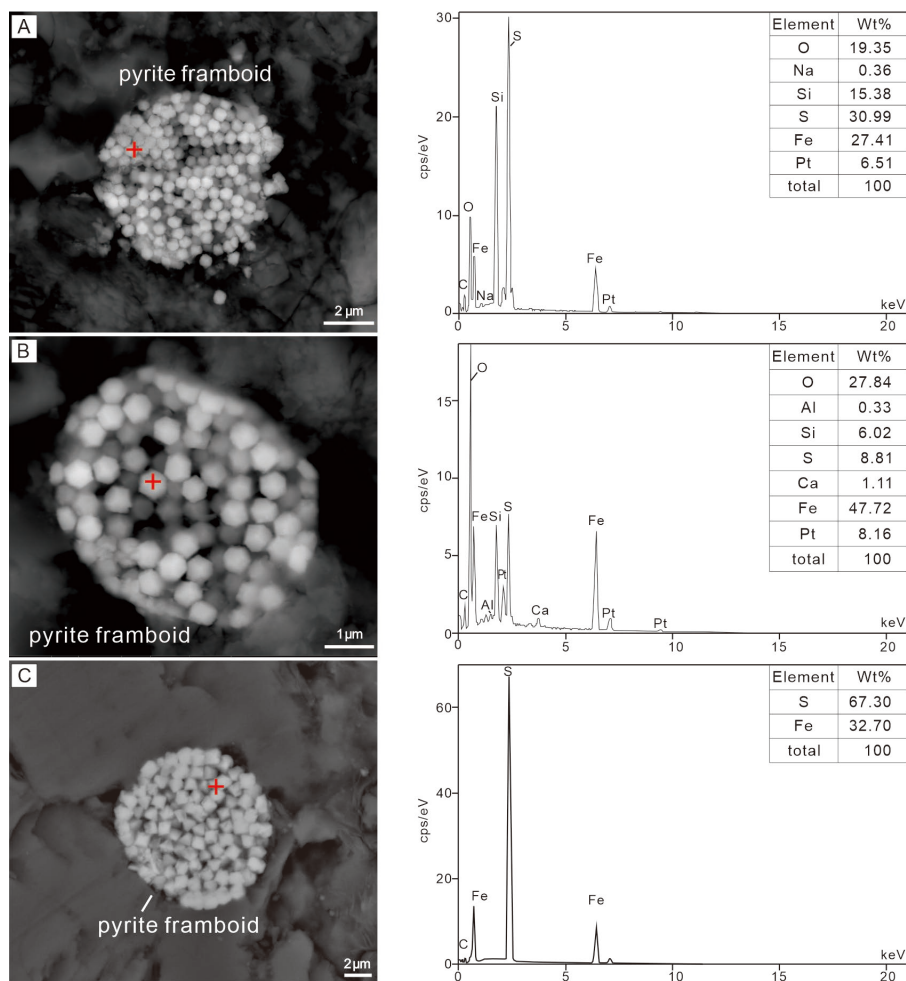


662 Figure 2. Stratigraphic log of the Ursula Creek section with total iron ( $Fe_T$ ),  $Fe_T/Al$ , iron proxies  
663 [ $Fe_{HR}/Fe_T$ ,  $Fe_{Py}/Fe_{HR}$ ,  $(Fe_{Py}+Fe_{ox})/Fe_{HR}$ ,  $Fe_{ox}/Fe_{HR}$ ], Mo and U concentrations, enrichment factors ( $Mo_{EF}$ ,  
664  $U_{EF}$ ) and their ratios ( $Mo/U$ ,  $Mo_{EF}/U_{EF}$ ), and pyrite framboid "box-and-whisker" plots. The "box"  
665 represents the interquartile range (25th–75th percentiles) of framboid diameters, the "whiskers" show the  
666 minimum and maximum values, and the central lines mark the median and the mean.



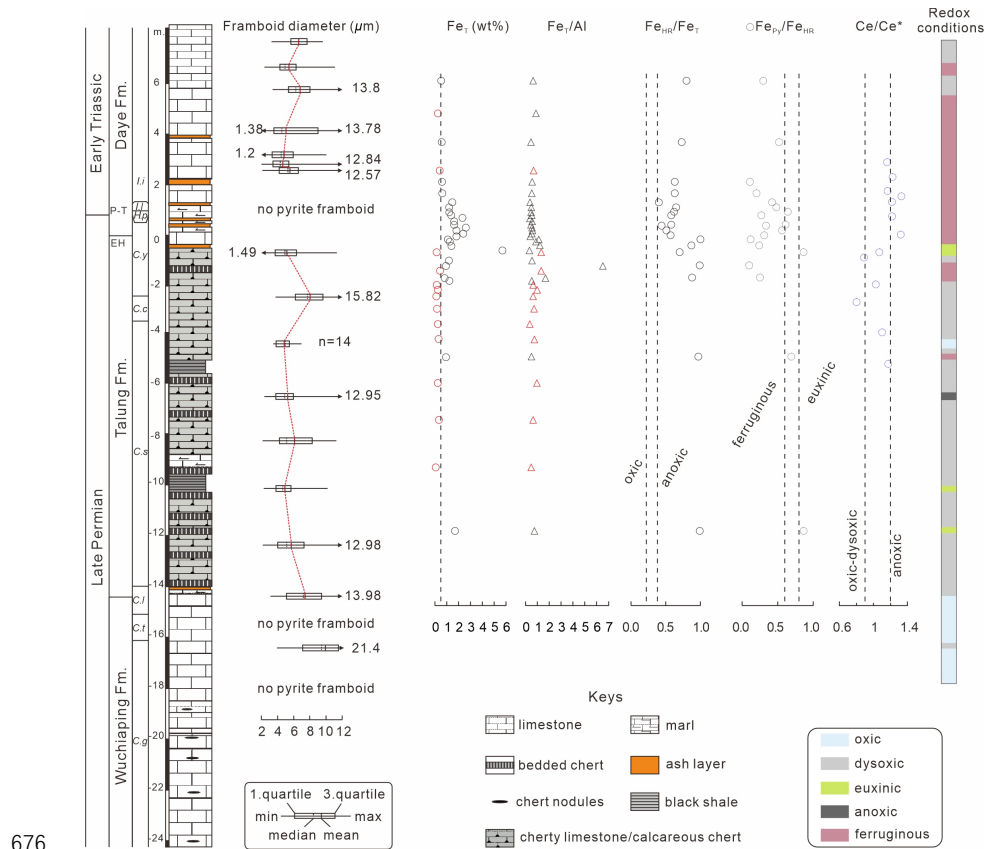
667

668 Figure 3. Mean diameter versus standard deviation of framboid size distributions for the Ursula Creek  
669 samples. The dashed line separates anoxic-euxinic from oxic-dysoxic conditions (cf. Wilkin et al., 1996).

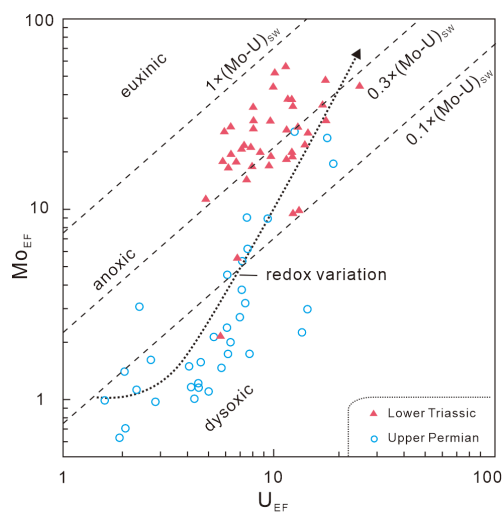


670

671 Figure 4. Mineral composition of pyrite framboids in samples from the Ursula Creek and Chibi sections.  
 672 (A) SEM image and EDS spectrum at the red cross of a pyrite framboid from the lower Fantasque  
 673 Formation, Ursula Creek; (B) SEM image and EDS spectrum at the red cross of a pyrite framboid from  
 674 the lower Grayling Formation, Ursula Creek; and (C) SEM image and EDS spectrum at the red cross of  
 675 a pyrite framboid from the lower Talung Formation, Chibi.

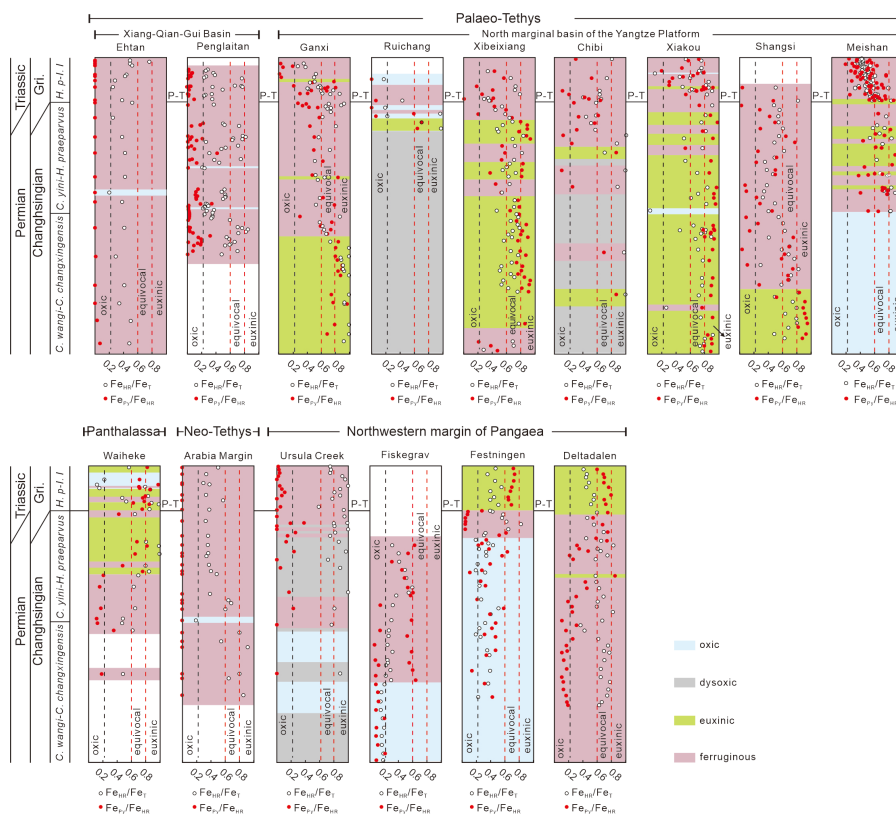


677 Figure 5. Stratigraphic log of the Chibi section with total iron ( $Fe_T$ ),  $Fe_T/Al$ , iron proxies [ $Fe_{HR}/Fe_T$ ,  
 678  $Fe_{Py}/Fe_{HR}$ ,  $(Fe_{Py}+Fe_{Ox})/Fe_{HR}$ ,  $Fe_{Ox}/Fe_{HR}$ ], Ce-anomalies, and pyrite framboid "box-and-whisker" plots.  
 679 Data of Ce-anomalies and framboids from Müller et al. (2023) and Yang et al. (2022) respectively.



680

681 Figure 6. Covariation of Mo and U across the P-T transition at the Ursula Creek section. The "redox  
682 variation" pathway represents progressive redox shifts from dysoxic to euxinic conditions (modified  
683 from Algeo and Tribovillard, 2009).



684

685 Figure 7. Palaeo-redox reconstruction via iron proxies across various sections situated in different  
 686 palaeogeographic settings. Data sources: Waiheke, Takahashi et al. (2021); Arabia Margin, Clarkson et  
 687 al. (2016); Ehtan and Ruichang, Yang et al. (2024); Penglaitan, Xiang et al. (2022); Ganxi, Lei et al.  
 688 (2017); Xibeixiang, Ge et al. (2022); Xiakou, Shen et al. (2016); Shangsi, Xiang et al. (2016); Meishan,  
 689 Xiang et al. (2020); Fiskegrav, Mettam et al. (2017); Festningen and Deltadalen, Schobben et al. (2020).  
 690 Gri. - Griesbachian; *H. p.* - *H. parvus*; *I. i.* - *I. isarcica*.